SAND2021-3529J

Development of a heterogeneous nanostructure through abnormal recrystallization of a nanotwinned Ni superalloy

Joel A. Bahena [a], Nathan M. Heckman [b], Christopher M. Barr [b], Khalid Hattar [b] Brad L. Boyce [b], and Andrea M. Hodge [a,c,*]

[a] Department of Aerospace and Mechanical Engineering, University of Southern California, Los Angeles, CA 90089, USA

[b] Sandia National Laboratories, PO Box 5800-1056, Albuquerque, NM 87185, USA

[c] Department of Chemical Engineering and Materials Science, University of Southern California, 3650 McClintock Ave., Los Angeles, CA 90089, USA

*Corresponding author. Tel.: +1 (213) 740 4225; fax: +1 (213) 740 8071; e-mail: ahodge@usc.edu

Abstract

This work explores the development of a heterogeneous nanostructured material through leveraging abnormal recrystallization, which is a prominent phenomenon in coarse-grained Ni-based superalloys. Through synthesis of a sputtered Inconel 725 film with a heterogeneous distribution of stored energy and subsequent aging treatments at 730°C, a unique combination of grain sizes and morphologies was observed throughout the thickness of the material. Three distinct domains are formed in the aged microstructure, where abnormally large grains are observed in-between a nanocrystalline and a nanotwinned region. In order to investigate the transitions towards a heterogeneous structure, crystallographic orientation and elemental mapping at interval aging

times up to 8 hours revealed the microstructural evolution and precipitation behavior. From the experimental observations and the detailed analysis of this study, the current methodology can be utilized to further expand the design space of current heterogeneous nanostructured materials.

Keywords

Nanotwins, abnormal recrystallization, heterogeneity, superalloys, nanostructured metals

1. Introduction

The design and development of heterogeneous nanostructured materials (HNMs) have garnered significant interest as these materials have demonstrated an improved strength-ductility synergy that has otherwise been lacking in monolithic nanocrystalline metals [1-4]. HNMs possess nanoscale features and domains of varying sizes that affect the dominant deformation mechanisms and generate inhomogeneous plastic deformation that promotes enhanced strain hardening and ductility. To control heterogeneity from the nanoscale to the macroscale, several processing and fabrication approaches have been implemented to generate heterogeneous structures. Techniques such as surface mechanical attrition treatment can produce gradient structures consisting of surface level nanoscale grains that gradually transition to a coarse-grained core [5]. Additionally, deposition techniques can offer an effective route for the synthesis of HNMs but with added intricacy [6, 7]. For example, a columnar structured Cu sample was electrodeposited with a consistent increase in columnar width and twin thickness, producing a hierarchically designed heterogeneous microstructure by tailoring deposition parameters [8]. However, utilizing electrodeposition restricts the available systems to single element or binary alloys [9], while using mechanical treatments localizes the nano-gradient to the surface. Nonetheless, the aforementioned

studies do provide the current framework for the design space of HNMs, even though the methodologies suffer from design limitations.

To date, most HNM studies have focused on generating gradient or bimodal structures, while more advanced heterogeneous designs, such as those with domains of varying grain morphologies (e.g. equiaxed, lamellae, columnar, etc.), residual stresses, or chemical composition have mostly been overlooked [5, 10, 11]. In order to synthesize more complex HNMs, there is a need for flexible techniques that can manipulate several variables and thereby induce both morphological and microstructural changes. An ideal candidate is magnetron sputtering, as it offers the capability of depositing nearly any metallic alloy while providing a wide range of deposition parameters that can be modified to tune the resulting microstructure and morphology. Parameters such as working distance, working pressure, and target polarization have a direct correlation with microstructural characteristics, which include feature size, texture, interface type, and residual stresses [12]. In addition to deposition parameters, material selection is another critical variable as physical properties can impact the microstructural features and morphology during film growth [13]. For instance, the stacking fault energy (SFE), which is an intrinsic material property, influences the propensity to form nanotwins [13]. Depending on the material or alloy selected, the aforementioned variables can present routes for controlling the microstructural evolution and potentially introduce heterogeneity in sputtered films [14-17]. An example of this is seen in age-hardenable Ni-based superalloys which are known to exhibit a bimodal grain size at critical temperatures and stored energies due to abnormal recrystallization [18-20]. In a study by Wang et al, it was observed that the annealing of a gradient-strained Ni-based superalloy with an initial

grain size of 2.39 μm resulted in the emergence of several abnormally large grains (ALGs) that reached sizes up to 208 μm at a critical distance [21]. The ability to tailor abnormal recrystallization in these materials to specific regions can potentially be leveraged with the microstructural control over nanoscale features and grain morphologies in magnetron sputtering. The result is an unconventional approach for the manipulation of a sputtered microstructure and design of a heterogeneous nanostructured superalloy.

In this work, age hardenable Inconel 725 films were synthesized via magnetron sputtering and subjected to an aging treatment that ultimately induced a transformation from a nanotwinned (NT) structure to an HNM with a unique and complex gradient grain topology. The aged microstructure contains domains consisting of columnar NTs, nano-grains, and ALGs with diameters greater than 1 μm, which presents a heterogeneous material with a wide range of grain sizes and morphologies. Microstructural transitions were highlighted by selecting specific aging times to provide insight into key thermally activated mechanisms and processes, with an emphasis in the region where abnormal recrystallization occurs. By combining crystallographic and elemental characterization, a thorough analysis of the grain evolution and precipitate formation was conducted. Overall, this work demonstrates a route to generate and tailor a unique sputtered superalloy that can further expand the current design space of HNMs.

2. Experimental

A 7.6 cm Inconel 725 target (Plasmaterials, Inc.) was magnetron sputtered onto 2.5 cm Corning Eagle 2000 glass substrate using a DC power supply. The nominal composition of the sputtered

film is provided in Table 1, which is in good agreement with the industry standard for Inconel 725 [22]. The sputtering conditions were set to a power of 1500 W, a working distance of 7.6 cm, and a working pressure of 2 mTorr, in order to achieve a sputtering rate of ~6 nm/s. The resulting film thickness was 15 μm, which was measured using an XP-2 profilometer. Prior to performing heat treatments, samples were peeled from the substrate to obtain free-standing films. Individual pieces of film were then aged in a GSL1100X tube furnace (MTI Corporation) at a constant temperature of 730˚C at intervals of 3, 5, and 8 hours under a vacuum pressure of $5x10^{-4}$ Pa. Upon completion of the aging sequence, samples were furnace cooled at a rate of ~5˚C/min.

Table 1. Composition of the sputtered film measured by EDS compared to the industry standard.

	Ni	Cr	Mo	Fe	Nb	Ti	Al
wt.% of sputtered sample	59.6	22.1	5.9	7.3	3	1.5	0.4
wt.% of standard Inconel 725 [22]	55-59	19-22.5	7-9.5	Bal.	2.75-4.0	1.0-1.7	0-0.35

Grain size and morphology evolution as a function of aging time were examined through electron back scattering diffraction (EBSD), providing a means to examine large cross-sectional regions of the film. Films were sandwiched in a split specimen mount (Ted Pella, Inc), mechanically polished, and ion milled using a Leica RES 102 ion polisher, allowing for cross sectional surface preparation. Scans were carried out in a JEOL IT300HRLV scanning electron microscope (SEM) with an EDAX Velocity high-speed detector at a working voltage of 30 kV, working distance of 20 mm, and step size of 20 nm. Furthermore, transmission electron microscopy (TEM) based automated

crystallographic orientation mapping (ACOM) was performed with a LaB_6 JEOL 2100 TEM operated at 200 kV with a step size of 3 nm to resolve nanoscale grains. Preparation of TEM lamellae was done by the focused ion beam (FIB) liftout method using a JEOL FIB – 4500, where the region of interest was protected from Ga beam damage through the deposition of a 1 μm-thick platinum protective layer. ACOM data was constructed with ASTAR NanoMEGAS software, and both EBSD and ACOM scans were analyzed using OIM software to obtain grain size statistics and crystallographic orientation information. EBSD data with confidence index lower than 0.1 were removed and shown as black pixels in the orientation maps. Segregation and precipitation behavior at the different time intervals were investigated with corresponding electron imaging and elemental maps gathered from a JEOL 2100F with both STEM and EDS capabilities (Oxford X-MaxN 100 TLE Windowless SDD).

3. Results and Discussion

A detailed analysis of the as-deposited Inconel 725 sample is shown in Figure 1. The cross-sectional microstructure of the sputtered sample is presented in the bright field STEM image in Fig. 1A showing a fully NT columnar structure (nanotwinned grains > 95%) where the arrow to the left of the image indicates the growth direction of the film. It should be noted that the formation of twins is mostly controlled by the material's stacking fault energy, which can be reduced with alloying [23]. High deposition rates can also help to induce favorable twinning conditions in high stacking fault energy materials such as Ni [24], leading to microstructures resembling the one observed in Fig. 1B, which highlights copious amounts of nanoscale growth twins perpendicular

to the growth direction of the film. The average columnar grain width was determined to be ~60 nm by measuring over 100 grains, where the distribution plot is presented in Fig. 1C. A uniform elemental distribution of key elements is shown in the individual EDS maps scanned from Fig. 1A in Fig. 1D, indicating the formation of a solid solution. Further characterization of the microstructure through ACOM mapping seen in Fig. 1E reveals that the film exhibits a strong texture in the (111) direction as indicated by the IPF triangle to the right of the figure.

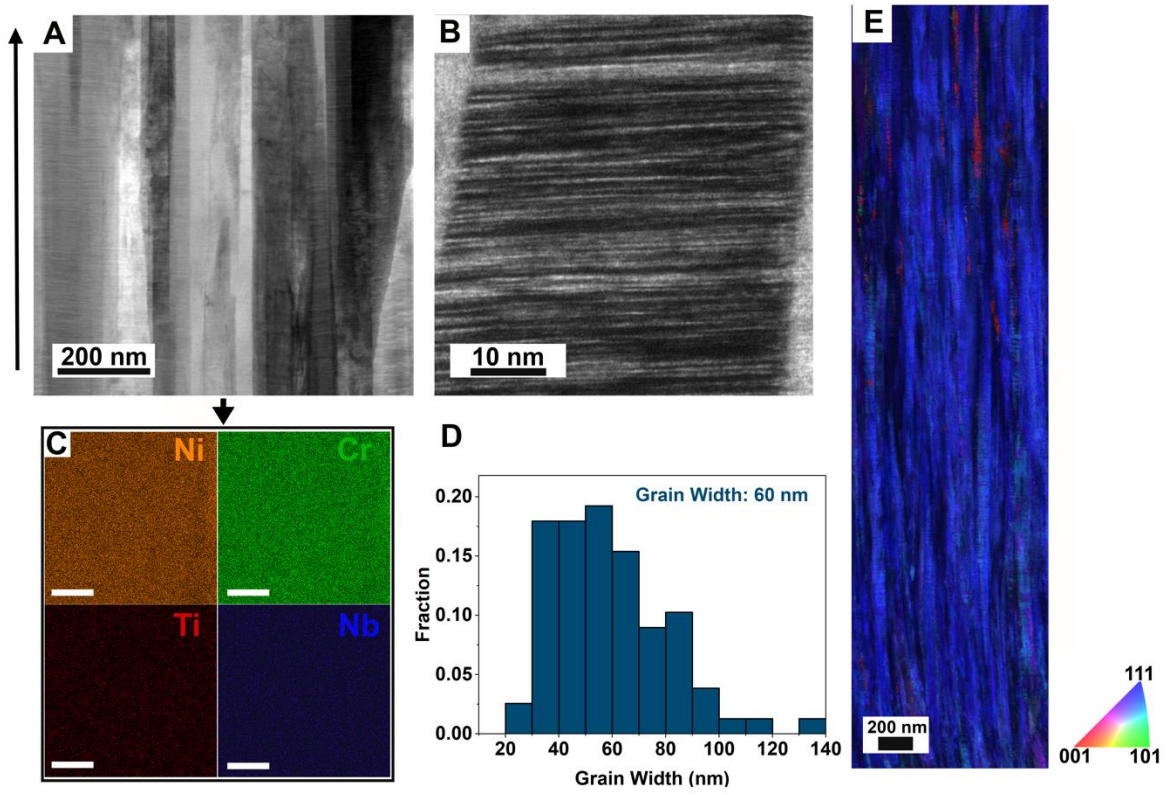

Fig. 1 (A) BF-STEM image showing the nanoscale columnar structure of the as-sputtered Inconel 725 sample, with (B) bright field TEM images highlighting density of nanotwins. (C) EDS maps of corresponding STEM image in (A) of Ni, Cr, Ti, Nb, (D) grain width distribution of columnar grains, and (E) ACOM map showing a strong (111) texture.

In addition to control over microstructural features, magnetron sputtering has the capability to develop stored energy gradients throughout the film thickness in the form of intrinsic stresses that can arise from impurities, grain boundaries, lattice misfit, voids, etc [25-30]. As discussed in the introduction, certain Ni-superalloys with low-moderate stored energy distribution will undergo abnormal recrystallization when annealed. This appears to be realized in a specific region of the current sputtered Inconel 725 film in Fig. 2 where the transformation from a NT microstructure to one composed of ALGs is depicted at different aging intervals. Thus, to determine potential sources for the observed heterogeneous behavior, it is necessary to understand the potential stored energy landscape of the NT sample in the as-deposited state. A common method in recrystallization studies to obtain a semi-qualitative representation of this data is through grain orientation spread (GOS) maps, which examine deviations in local misorientations [21, 31, 32]. Specifically, for abnormal recrystallization, it has been reported that ALGs emerge in heterogeneous regions with low-moderate stored energy and GOS, which can promote the formation of a limited number of stable nuclei that grow at the expense of higher energy grains. [19, 21, 31]. For the purpose of microstructural visualization, Fig. 2A shows a representative cross-section schematic of the as-sputtered sample, to indicate where GOS analysis was performed. Fig. 2B, shows the GOS map from the ~5 μm representative area outlined in green, which was obtained from the ACOM data presented in Fig. 1E. To the right, distribution plots of the orientation spreads are displayed along three different regions of the highlighted area. The GOS spread is colored from 0˚ to 5˚, where previous studies have indicated that grains with larger orientation spreads are inclined to have higher stored energy [33]. The transition in color of the map and shift in distribution plots point to grains with higher GOS values being located towards the bottom of the

region, whereas grains with lower GOS values are seen towards the top. This gradient would suggest that the stored energy in the film decreases along the growth direction [34]. The source for the inhomogeneous distribution of presumed stored energy can be attributed to strain induced by lattice misfit between the substrate and film, in combination with defects generated by atomic peening that are more prominent in the early stages of film growth [27, 28]. Furthermore, grain boundary energy anisotropy induced by grains which deviate from the preferred (111) orientation can generate sharp gradients in stored energy [35, 36]. Overall, it is estimated that the ~4 μm region delineated by blue lines in Fig. 2A exhibits the heterogenous distribution of low-moderate stored energy required for abnormal recrystallization to occur, as seen in other studies [31]. As such, this particular region of interest will be referred to as the "AR region" throughout the manuscript.

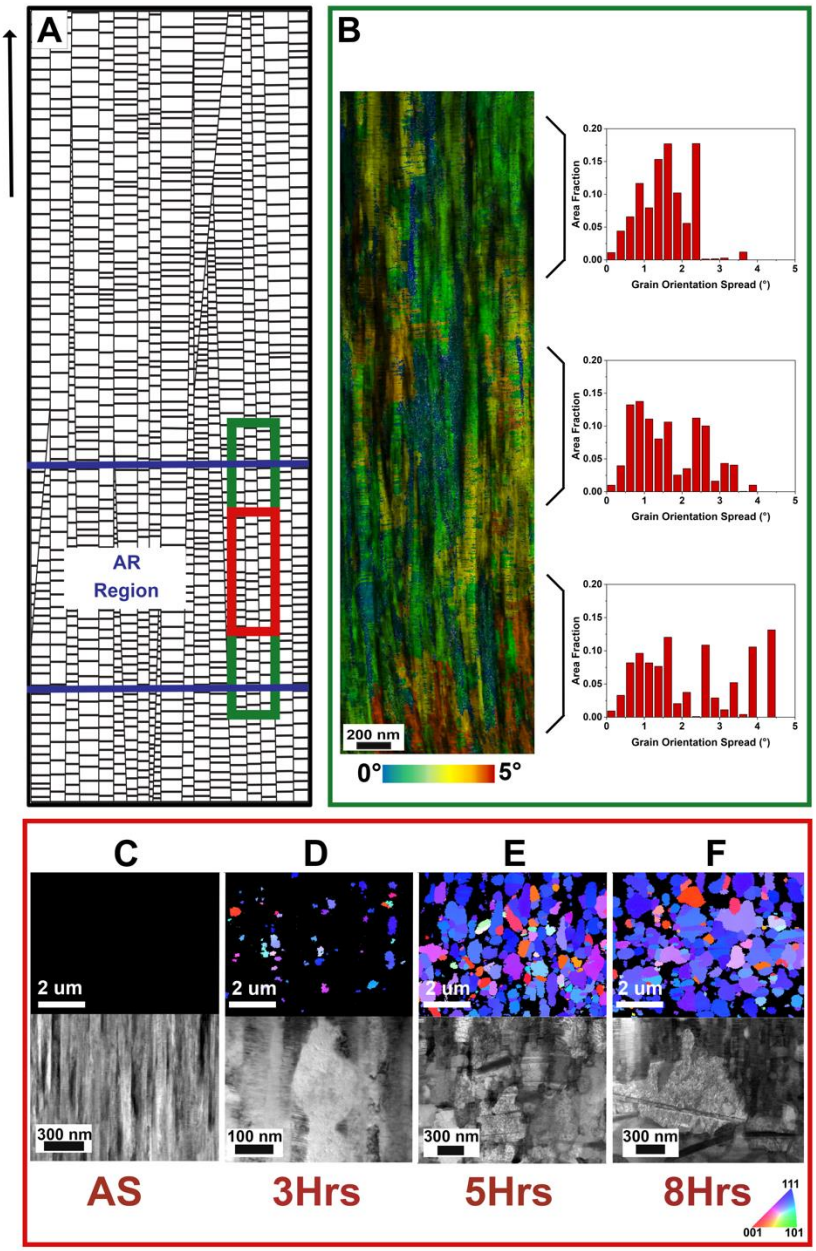

Fig. 2 (A) Schematic of a representative cross-section of the as-sputtered film highlighting the region expected to undergo abnormal recrystallization delineated by blue lines. Growth direction is shown by arrow to the left. This region includes a green rectangle representing (B) and a red rectangle representing (C-F). Where (B) shows the GOS map and corresponding distribution plots, which reveals a gradient in GOS. (C-F) highlight the EBSD scans (top) and BF-STEM images (bottom) representing the microstructural evolution of the abnormal recrystallization region in (C) the as-sputtered condition and after aging treatments of (D) 3 hours, (E) 5 hours, and (F) 8 hours. IPF triangle is shown to the bottom right of the scans.

Cross-sectional EBSD and STEM imaging of the AR region are presented for three aging times of 3,5, and 8 hours at 730˚C in Figs. 2C-F, which highlight the development of larger grains. While this conventional EBSD technique does not readily resolve the NT structure or nanoscale features as indicated by the low-index (black) regions in the scans, it allows for the isolation of ALGs from the original as-sputtered microstructure. Previous studies have mainly observed abnormal recrystallization near the γ′ solvus (~1000˚C), however, it was expected that the nanostructured nature of the sputtered film would cause recrystallization to occur at lower temperatures [35, 37]. Furthermore, the selected temperature would allow for a comparison of the precipitation behavior with coarse-grained Ni-superalloys, which typically form γ' and γ'' precipitates under similar conditions [38], but traditional formation of these phases was not observed. Meanwhile, the characterization of the microstructures at the selected aging times were guided by structural changes detected through XRD that is provided in Supplementary Information. The use of interval aging times allowed for key microstructural transitions to be captured through ACOM and EDS, enabling the investigation of thermally activated mechanisms and precipitation behavior. Through the combination of these techniques, a detailed analysis of the transformation from a NT alloy to an HNM is presented in the following sections with an emphasis on the labeled AR region.

3.1. Three Hour Heat Treatment: Initial AR and Cr Segregation

After a 3-hour aging treatment, subtle but critical changes to the microstructure are observed. In comparison to the as-deposited state (Fig. 2C), cross-sectional EBSD scans reveal the emergence of a few larger grains in Fig. 2D. Likewise, the representative STEM image shows a twin-free

grain that has consumed the neighboring columnar structure. The development of these grains with distinct morphologies was constrained to the AR region that is likely a function of a stored energy gradient throughout the thickness of the film [35]. Namely, the site-specific changes in the microstructure are presumed to be driven by the heterogeneous distribution of low-moderate stored energy in this region, that can drive a nucleation limited recrystallization process [21]. While it is difficult to determine the process responsible for the emergence of ALGs at the current aging time, the parallels seen with previous studies strongly indicate the initiation of abnormal recrystallization [19, 21, 31]. Despite the minor changes in the AR region, the overall microstructure remains predominantly a NT structure as can be seen in the STEM image of the upper portion of the film in Fig. 3A. There are, however, several globular particles that are decorating the columnar grain boundaries. The EDS maps in Fig. 3B, which highlight Ni (orange) and Cr (green), reveal that these precipitates are rich in Cr. Based on the high Cr content of this alloy, low ageing conditions and observations from previous studies, it is assumed that the Cr-rich precipitates dispersed throughout the microstructure are $M_{23}C_6$ carbides [39]. Other common carbide formers, such as Mo, were also examined, but these elements appear to remain in solid solution under the current conditions. To further examine the segregation behavior, ACOM was performed to identify the grain boundary character of several columnar grains as solute segregation has been shown to be highly dependent on boundary energies [40]. The scan presented in Fig. 3C was utilized to identify preferential sites for Cr segregation, where the grain boundaries in the green bordered insets were analyzed. The red-dotted lines indicate high angle grain boundaries with misorientations greater that 15°, while the white dashed lines indicate low angle and coincident site lattice grain boundaries. Cr-rich precipitates were identified and outlined by dotted yellow lines, which were

verified with corresponding STEM images. Over 20 boundaries were examined (inset), where the $M_{23}C_6$ precipitates appear to form preferentially along high angle grain boundaries, with no identifiable precipitates along low angle or coincident site lattice grain boundaries. In coarse grained Ni-superalloys, it has been reported that the enhanced diffusion pathways and increased energy of high angle grain boundaries leads to preferential segregation of Cr and C [40], which is in agreement with our current observations. The formation of these Cr-C precipitates could also lead to improved thermal stability by impeding grain boundary migration, and as a result influence the microstructural evolution at longer aging times [41]. While it is difficult to predict if the $M_{23}C_6$ precipitates formed prior to the formation of the ALGs, secondary-phase particles can heavily affect the recrystallization rate [35]. Additionally, given the time and temperature dependency on recrystallization and grain growth, it can be assumed that there lacked sufficient time for further growth of the newly formed grains. Overall, the 3-hour aging treatment captures the formation of the early stages of abnormal recrystallization and Cr segregation.

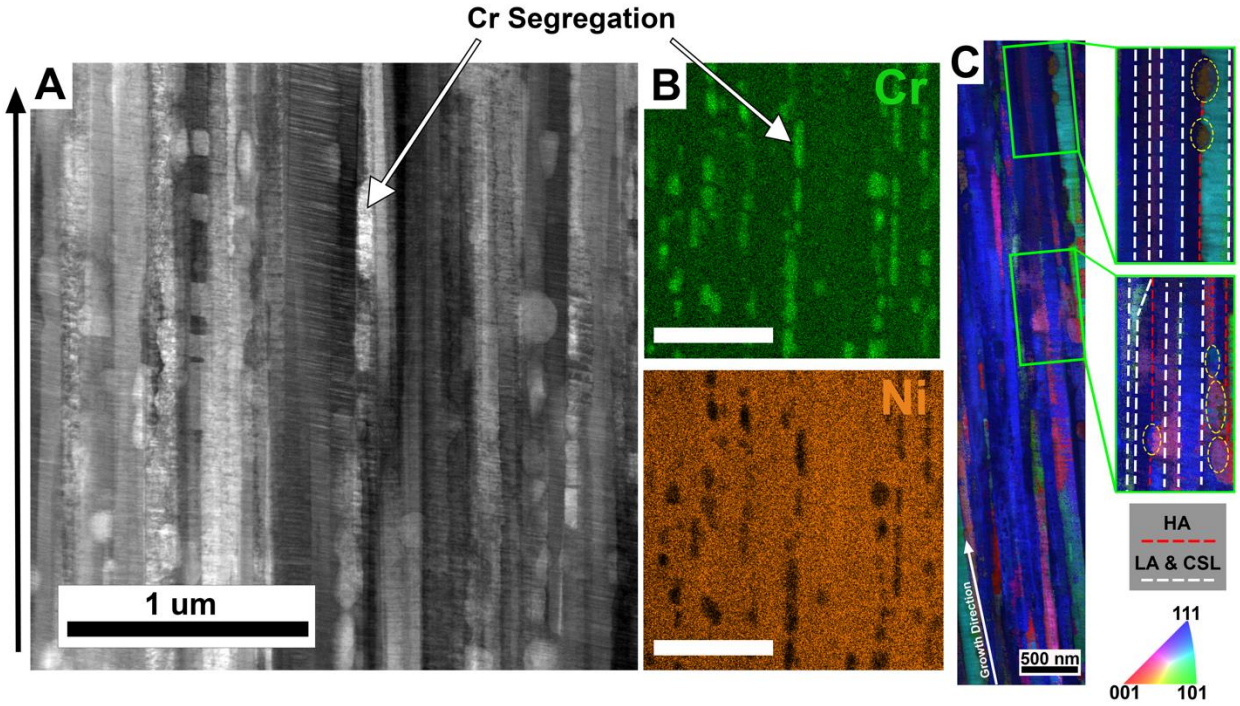

Fig. 3 (A) BF-STEM image of the 3-hour aged sample of the upper portion of the film and (B) corresponding EDS maps highlighting Cr segregation where white scale bars are 1μm. (C) ACOM scans of representative region, where green insets highlight select GBs with red dotted lines indicating HAGBs and white dotted lines indicating low angle (LA) GBs and coincident site lattice (CSL) GBs. Cr precipitates are encircled with yellow dotted lines. IPF triangle is shown to the right of the scan.

3.2. Five and Eight Hour Heat Treatments: Heterogeneous Nanostructured Material

Upon aging at 5 and 8 hours, there is a transition to an HNM as illustrated through cross-sectional EBSD scans of the film shown in Fig. 4A. For visualization and comparison purposes, the areas below and above the AR region are presented in this figure. The three distinct regions shown for both aging times consists of a (i) NT region containing nanoscale columnar grains with a high density of stabilized nanotwins; (ii) the AR region where ALGs have formed and undergone grain

growth; and (iii) a nanocrystalline region where equiaxed grains have formed. These microstructural transitions are highlighted in Fig. 4B, where the feature sizes of the as-sputtered, 5 hour, and 8 hour samples are plotted along the thickness of the film. These observations are consistent with the expectation that the sputtered film exhibits a residual stress and stored energy gradient that would govern the formation of distinct microstructural regions [21]. The three regions comprise an overall complex microstructure with each region undergoing discrete thermal processes, and in this study the microstructural analysis at these select aging times focuses primarily on the AR region (ii) although regions (i) and (iii) will also be briefly discussed. For region (i), the lower stored energy towards the upper portion of the film does not sufficiently drive recrystallization, leading to a similar NT structure as seen after the 3-hour aging condition. Other NT Ni alloys, such as Ni-Mo-W, have shown similar thermal stability under comparable temperatures due to the low enthalpy stored in twin boundaries and Zener drag forces generated from secondary phase precipitates [14]. Hence, the high density of nanotwins and Cr-carbides along grain boundaries of the aged sputtered Inconel 725 sample similarly stabilize the NT structure in region (i). Despite the lower stored energy, a few ALGs do appear in this region, as seen in the EBSD scans in Fig. 4, and are likely associated with localized stored energy variation generated during the sputtering process. In contrast, region (iii), which should exhibit the highest stored energy due to its vicinity to the bottom of the film, has a sufficient density of stable nuclei sites that induce complete recrystallization and a smaller grain size [21, 32]. As a result, nanoscale equiaxed grains are formed with Cr-carbides located along grain boundaries, potentially minimizing further growth. As can be seen from the insets in Fig. 4, the microstructural features in region (i) and (iii) showed minimal changes between the aging treatments of 5 and 8 hours.

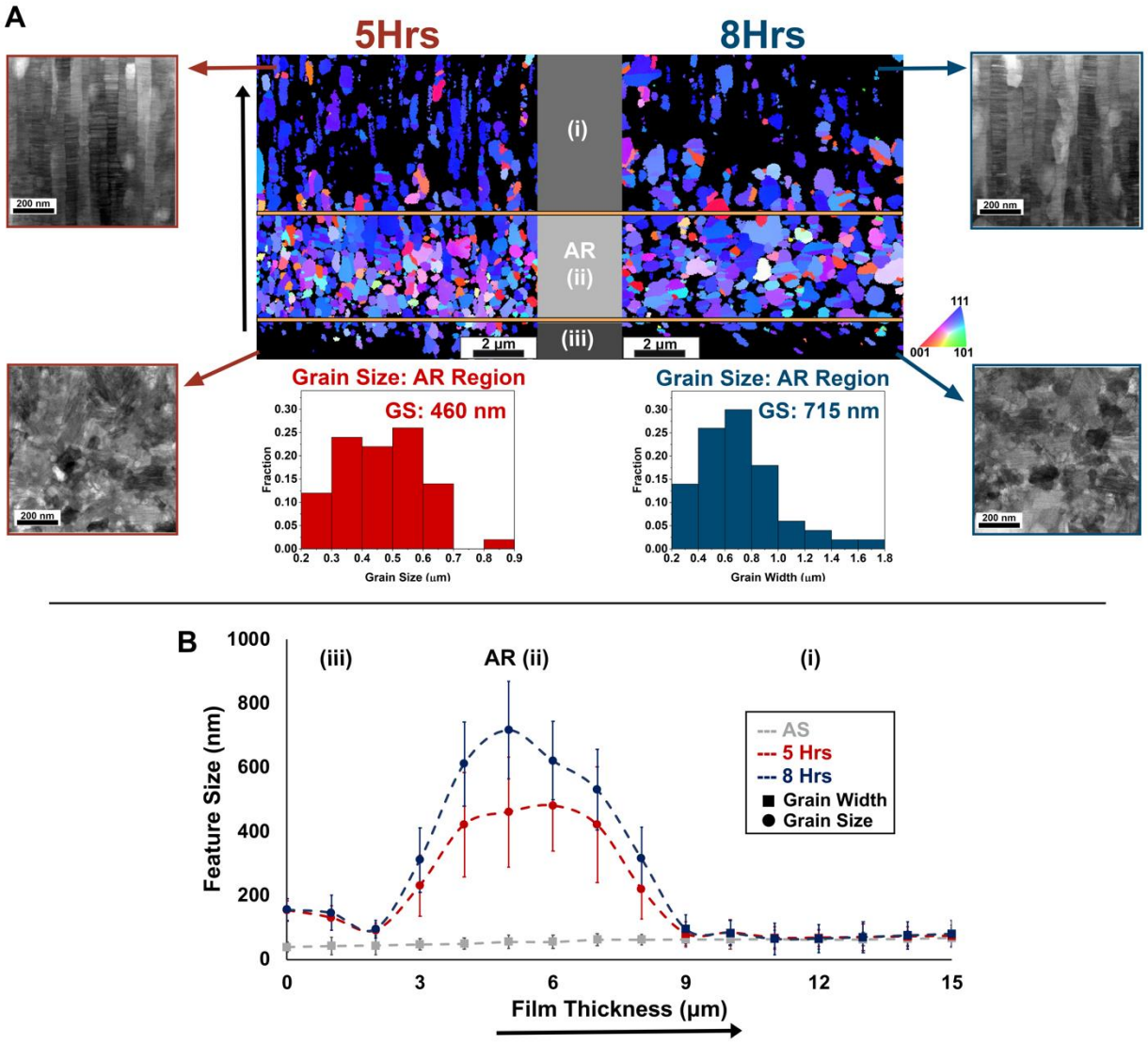

Fig. 4 (A) EBSD maps of cross-section of heterogenous structured achieved at aging times of 5 and 8-hours (top) with respective grain size distributions of grains in the AR region (ii) (bottom). Insets highlights characteristic microstructures of the region (i) and region (iii) at the different aging times. IPF triangle is shown to the right of the scans. (B) Feature size is plotted as a function of film thickness for films in the as-sputtered (AS) condition (grey), and after aging at 5 (red) and 8 Hrs (blue), where filled squares indicate columnar grain width measurements and filled circles indicate equiaxed grain size measurements. The arrows indicate the growth direction of the film.

In the labeled AR region (ii), which as seen in Fig. 4 spans ~4 μm and is observed in between region (i) and (iii), the NT structure is quickly replaced by ALGs. The EBSD scans and grain size distribution plots in Fig. 4A show differences in morphology and an increase in average grain size from ~460 nm and ~715 nm after 5 and 8 hours, respectively. To investigate the effects of stored energy and the microstructural changes in the AR region (ii) at these two aging times, correlative STEM, ACOM, and EDS maps at each interval are presented in the following sections.

3.2.1. AR Region: Five Hour Treatment

In order to examine the microstructural and precipitate evolution in detail, ACOM and EDS analysis of two different sections in the AR region after the 5-hour aging treatment are presented in Fig. 5 and Fig. 6, respectively. Specifically, Fig. 5 presents a corresponding STEM image (Fig. 5A) and ACOM map (Fig. 5B) which give insight into the grain morphology and orientation of the observed microstructure, where the arrow on the left indicates the growth direction of the film and is also an indication of the direction of decreasing stored energy. The IPF triangle on the right reveals the crystallographic orientations of the grains seen in the ACOM scan. In Fig. 5A-B, several grains with random orientations and different morphologies compared to the surrounding (111) oriented grains are outlined with dashed lines. The distinct characteristics between the highlighted and non-highlighted grains provide evidence of two thermally activated processes invoking the increased grain size and formation of ALGs. The changes in orientation of the highlighted grains suggests that a nucleation-based recrystallization is driving the growth of select grains. As previously indicated by the GOS map in Fig. 2A, this region should exhibit areas of

moderate stored energy, which restricts the number of stable nuclei that can form and grow, analogous to the hypothesized theory of abnormal recrystallization in other Ni-superalloy studies [18, 32]. The newly formed low stored energy grains then grow at the expense of surrounding pre-existing grains with higher stored energy, leading to the eventual emergence of ALGs [32]. Additionally, the new grains generated through recrystallization appear to promote the formation of annealing twin boundaries, where select boundaries are outlined in red in Fig. 5B. Similar observations have been reported in studies of thermo-mechanically processed Ni alloys, where twinning occurs during the growth process after recrystallization [42-44].

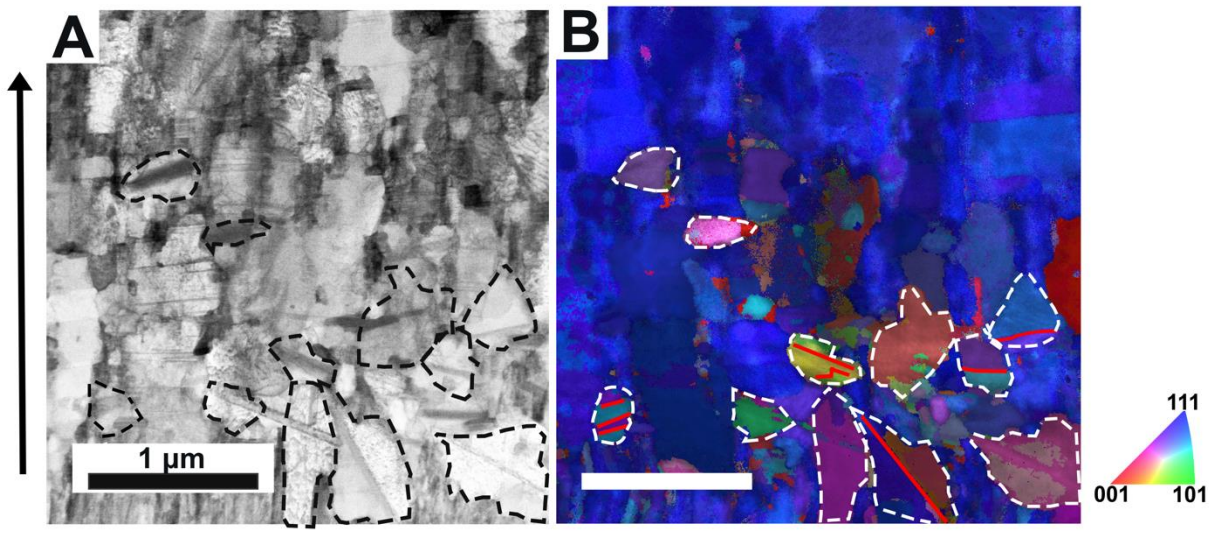

Fig. 5 (A) BF-STEM images and (B) corresponding ACOM scans of the AR region in the 5-hour aged sample, highlighting ALGs governed by different thermal processes. Randomly oriented recrystallized grains are highlighted by dashed black and white lines. White scale bar is 1 µm and IPF triangle is shown to the right of the scan.

Concurrently, several ALGs with a slightly rectangular morphology are observed in Fig. 5A, with the ACOM map in Fig. 5B revealing an evident (111) orientation, identical to that of the as-deposited film. The orientation and observed morphology suggest that these grains develop through the detwinning and coarsening of columnar grains in a direction perpendicular to the growth direction of the film [17, 45]. Considering that the NT structure in region (i) did not undergo similar transitions, the source of this increased twin and grain boundary mobility can be attributed to the low-moderate stored energy specific to the AR region. Thus, the microstructural changes denote a strain induced boundary migration (SIBM) process, facilitated by variations in stored energy causing boundaries of low energy grains to move towards high stored energy regions. As a result, low stored energy regions are generated with the same crystallographic orientation as the parent grain [46]. While the driving force for recrystallization and SIBM are similar, the differences in resulting microstructures are considerable as seen by the distinct types of observed grains. Notably, both processes are dependent on the initial stored energy state, where SIBM typically occurs at lower stored energy conditions than nucleation-based recrystallization [47].

The heterogeneous distribution of stored energy not only leads to variation in grain morphology and orientations but also in precipitation behavior. Fig. 6 highlights the distribution of precipitates including corresponding STEM and EDS maps. Throughout the entire region, $M_{23}C_6$ precipitates are observed in addition to rafted structures and δ precipitates, where arrows in Fig. 6A mark individual examples of each. The rafted structure as indicated by the purple arrow, is primarily observed in the upper portion of the film in the square shaped grains the have undergone SIBM.

This type of structure is typically observed in single crystal Ni-superalloys [48, 49] and is the product of the discontinuous precipitation of γ and γ' that can be driven by local reductions in chemical free-energy, decreases in stored energy, or grain boundary migration [50, 51]. Thus, it can be deduced that the observed rafting was likely promoted during the SIBM process. In contrast, the recrystallized ALGs towards the bottom of the film contain elongated plate shape particles across the width of the grain as indicated by the blue arrow. The EDS maps in Fig. 6B show that these particles are rich in Nb and Ti indicating the formation of the Ni_3(Nb,Ti) δ phase. This was further validated with an SAED pattern from the [111] matrix zone axis shown in the inset, revealing the presence of [100] δ superlattice reflections [52]. While δ phase has been observed in Ni-based superalloys under similar experimental temperatures, it typically requires much longer aging times to form. For example, an Inconel 718 sample aged at 750˚C required 100h for noticeable precipitation of δ phase [53]. However, it has been demonstrated that increasing the stored energy through plastic deformation with techniques such as cold rolling can accelerate precipitation kinetics at lower temperature [54]. Therefore, it is likely that the higher stored energy that governed recrystallization also promoted the rapid precipitation of δ phase. From the STEM images it appears that precipitation of δ phase occurs intragranularly, but through comparing the ACOM scan and EDS maps it is revealed that many of the δ precipitates are located along annealing twins. Due to the low grain boundary energy associated with twin boundaries, precipitation at higher energy sites would be expected, but several studies have identified twin boundaries as nucleation sources for δ precipitates as a function of the good matching between the twin boundary plane and δ habit plane [52, 53, 55]. Moreover, the formation of δ phase is typically associated with a transformation from metastable γ'' which was not identified in this study. Direct

phase transformation of a similar phase has been observed in a NT Haynes 242 sample upon aging, which was attributed to the presence of HCP-like ordering [23]. Nonetheless, an HCP structure was not apparent from our observations, thus, it is unclear whether the δ phase is the byproduct of phase transformation or direct precipitation.

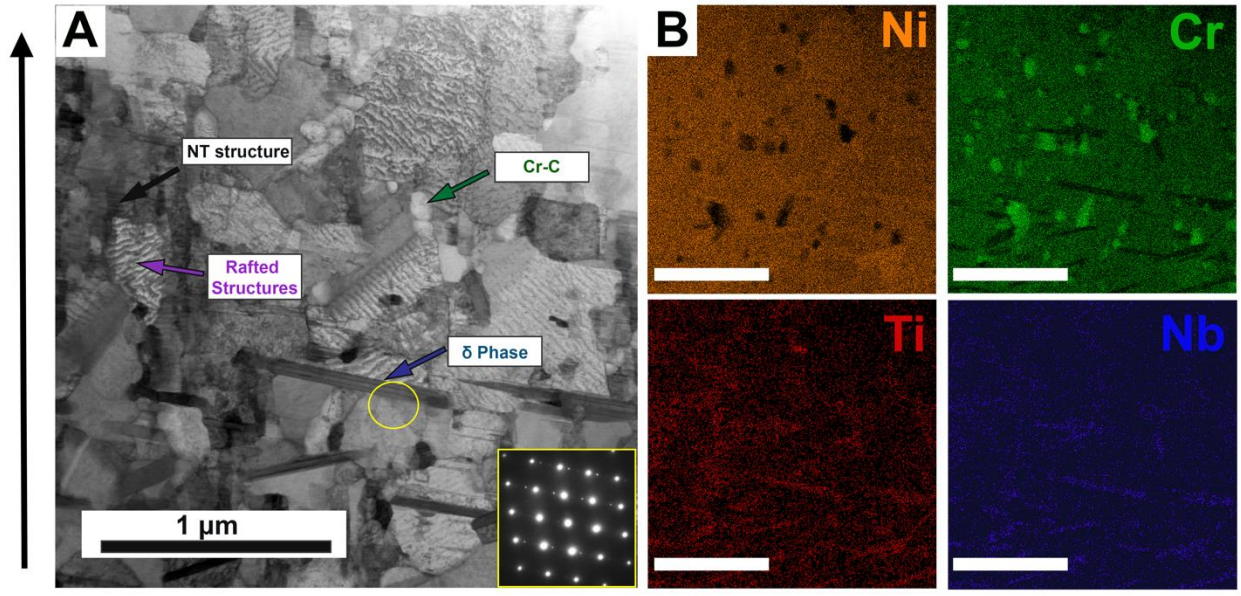

Fig. 6 (A) BF-STEM image of the 5-hour aged sample illustrating the heterogenous precipitate and microstructural behavior in the AR region with inset SAED pattern confirming the presence of δ precipitates. (B) EDS maps of Ni, Cr, Ti, and Nb highlighting location of different precipitates where white scale bars are 1 µm.

Overall, the 5-hour treatment causes both a SIBM and a nucleation-based recrystallization process to occur in the AR region of the film, giving rise to the formation of different types of ALGs with distinct precipitate behavior. The stored energy advantage of ALGs has been shown to overcome Zener pinning forces and the same is shown in this study, as both types of grains exhibit growth

despite the high density of Cr-C precipitates decorating the grain boundaries [32]. It is still expected that the pinning precipitates would promote sluggish kinetics that lower the overall grain growth rates [56]. Furthermore, unconsumed NT columnar grains (black arrow) are seen throughout this region suggesting that certain columnar grains exhibited initial low stored energy as they are unaffected by either thermal process. Thus, the stored energy profile appears to heavily influence the AR region, producing a more complex overall microstructure with higher levels of order.

3.2.2. AR Region: Eight Hour Treatment

After the 8 hour treatment, further coarsening of recrystallized ALGs is observed throughout the AR region with a more homogeneous distribution of precipitates as detailed in Fig. 7, which presents similar STEM, EDS, and ACOM analysis as performed in the previous section. In Fig. 7A, a STEM image depicts an area between region (i) and the AR region (ii), where the transition is highlighted by a dashed white line, and the arrow to the left indicates the growth direction of the film. From the image, it can be seen that the equiaxed grains have increased in size and are more prominent towards the upper portion of the AR region. Accompanied with the EBSD scan from Fig. 4, it is apparent that this morphology is more pronounced in this region of the film, indicating that the increased aging time has allowed for further growth and the formation of new recrystallized grains. NT columnar grains are also still observed in this region as denoted by the black arrow in Fig. 7A. In terms of precipitates, a higher density of δ phase are present as a result of the increased number of recrystallized ALGs. The EDS maps in Fig. 7B show the elemental

distribution of key elements of the corresponding area, where the δ phase can be identified by a Nb enrichment. $M_{23}C_6$ are still also observed, where the Cr map in Fig. 7B illustrates the distribution of these precipitates along grain boundaries. Furthermore, the rafted structure is no longer observed after the 8 hour treatment as the SIBM grains appear to have been consumed. The crystallographic orientation data of the region enclosed by the orange box is presented in the ACOM map in Fig. 7C. Similar to the observations after the 5-hour aging treatment, the recrystallized ALGs have formed annealing twins, where select twin boundaries are outlined in red. Coincidentally, a large fraction of δ precipitate are observed on or near annealing twin boundaries.

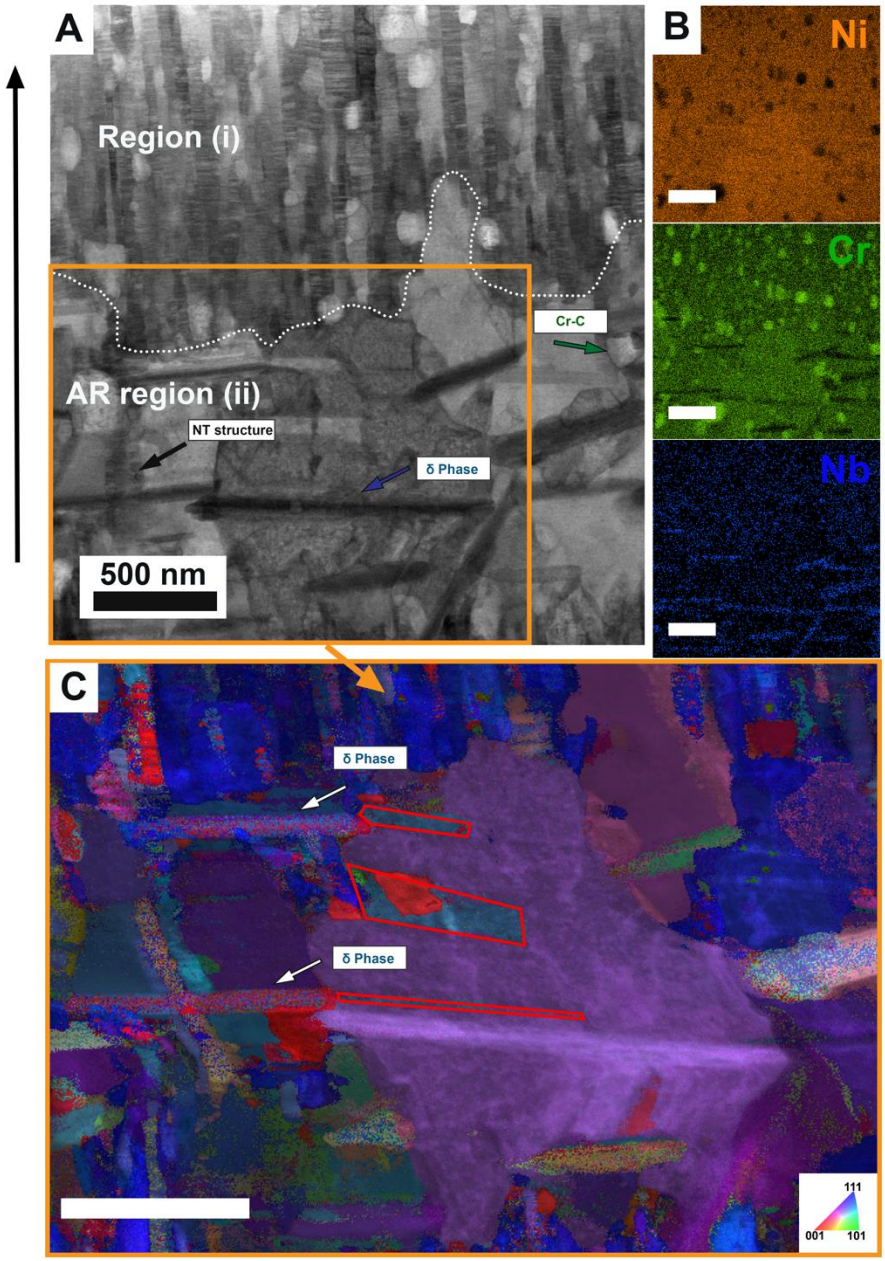

Fig.7 (A) BF-STEM Image, corresponding (B) EDS maps of Ni, Cr, Nb, and (C) ACOM maps from the outlined (orange) region in (A) with inset of IPF triangle of the 8-hour aged sample. White scale bars are 500 nm.

The observed microstructure points to the continued evolution and growth of the recrystallized grains as the primary source for the increased size of ALGs at 8 hours. This shift is likely attributed to a stored energy difference, as it is anticipated that the recrystallized grains would exhibit lower energy and preferentially grow at the expense of SIBM grains. Meanwhile, the presence of NT columnar grains reaffirms that certain grains are deposited at an initial low stored energy state. As indicated by the continued growth of ALGs, the extra aging time has allowed for sufficient mobility to overcome sluggish kinetics due to drag forces generated by secondary phases at grain boundaries, such as $M_{23}C_6$ and δ precipitates [55, 56]. Consequently, this has also led to an increased density of δ phase that, as previously discussed, is driven by stored energy and the formation of annealing twins. Through comparing STEM, EDS, and ACOM, several δ precipitates are seen on or near annealing twin boundaries, providing further evidence of that as a preferential precipitation site. Effectively, the observed microstructure after the 8 hour treatment presents a natural progression from the one seen after 5-hours. Previous studies have shown that during abnormal recrystallization, there is a time dependency until the eventual mutual impingement of select equal energy grains. This in turn, leads to a more homogeneous distribution of ALGs, as the lowest stored energy grains will dominate the resultant microstructure [21, 32]. Likewise, the recrystallized ALGs with δ precipitates comprise the majority of the AR region.

Altogether, the observed microstructures of the aged sputtered samples demonstrate a significant contrast with that of traditional Inconel 725 that could lead to attractive mechanical behaviors [22, 57]. The absence of conventional γ′ and γ″ is especially notable. As previously discussed, it is expected that the increased stored energy in the AR region (ii) facilitates either an accelerated or

a direct formation of δ phase along annealing twins and grain boundaries. The presence of intergranular δ precipitates have been shown to lower the yield strength of aged Ni-superalloys while improving ductility [58]. However, given the high density of nanotwins in region (i), which are known to promote exceptional strength [14, 59, 60], the absence of traditional γ' or γ'' precipitates is not expected to diminish the properties of the presented alloy. Similarly, the formation of a heterogenous structure containing three distinct domains with variable grain size, precipitate formation, and morphologies could lead to a strength-ductility synergy that has been observed in other HNM studies [2]. The NT structure of region (i) and nanocrystalline structure in region (iii) would significantly strengthen the material, whereas the AR region (ii) could provide a ductile interior that can accumulate dislocations during deformation [1]. It is possible that these attributes would also translate to enhanced tribological properties as the ductile core could suppress strain localization and crack propagation [61]. In this regard, it would be interesting to examine the structure-property relationship of the observed heterogeneous microstructure after the 5 and 8 hour heat treatments in future studies.

4. **Summary and Conclusions**

In this study, a novel approach for producing a HNM was developed, inspired from the heterogeneous behavior observed in CG Ni-based superalloys and translated to the nanoscale by annealing a sputtered NT structure with heterogeneous distribution of stored energy. The resulting microstructure consisted of three distinct regions that were influenced by the stored energy profile of the film, presenting a unique combination of grain morphologies and sizes that has not been

previously observed. A graphical summary of the microstructural evolution during the aging process is depicted in Fig. 8. While the three regions are presented, the complex nature and heterogeneous evolution of the microstructure prompted the current study to mainly focus on the thermal processes governing the changes in the AR region (ii). The microstructural analysis revealed that development of ALGs in this region is induced by both a nucleation-based recrystallization and a SIBM process. Furthermore, different grain sizes and precipitation behavior are observed after 5 and 8 hours, demonstrating the potential to tailor the AR region and the overall HNM depending on aging time. Future studies are needed to further elucidate the processes occurring in region (i) and (iii) as well as to investigate the effects of domains with varying morphological features and size on the mechanical properties.

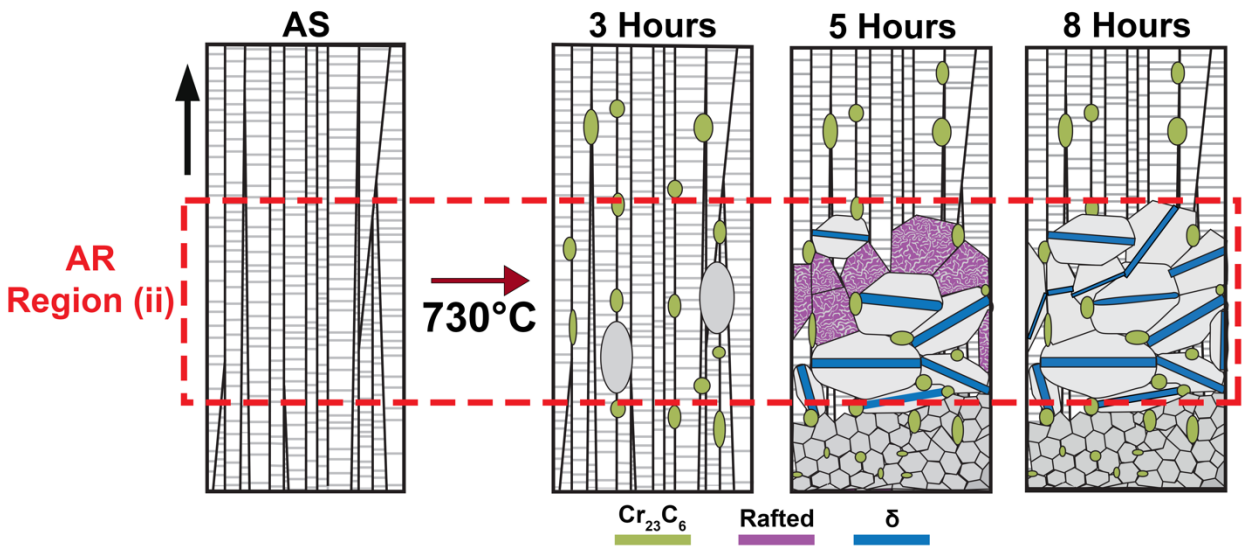

Fig. 8 Schematic overview of the microstructural evolution of the sputtered Inconel 725 film at different aging times that presents the changes in grain morphology, precipitate formation, and development of a heterogenous microstructure. The arrow to the left indicates the growth direction of the film and the red dotted box highlights the AR region.

Overall, this study validates the proposition of combining the flexibility of magnetron sputtering with a Ni-based superalloy to produce a unique HNM which can be further modified. Through controlling factors such as the distribution of stored energy during the deposition process, this approach could be utilized to tailor different domains and generate more complex microstructures. In addition to the phenomenon of abnormal recrystallization being prevalent in Ni-based superalloys, it has also been observed in Co-based superalloys [62] which provides opportunities to explore different microstructural designs and alloy combinations. Thus, the current methodology provides a potential path to expand the current design space of nanomaterials.

Acknowledgements

AMH was supported by the National Science Foundation under Grant DMR-1709771 and the Office of Naval Research under grant N00014-18-1-2617. NMH, CMB, KH, and BLB were supported by the United States Department of Energy, Office of Basic Energy Sciences (BES), Division of Materials Science and Engineering. JAB was supported by the NSF and ONR grants during the academic calendar and by the BES grant during the summer. This work was performed, in part, at the Center for Integrated Nanotechnologies, an Office of Science User Facility operated for the U.S. Department of Energy (DOE) Office of Science. Sandia National Laboratories is a multi-mission laboratory managed and operated by National Technology and Engineering Solutions of Sandia, LLC, a wholly owned subsidiary of Honeywell International, Inc., for the U.S. Department of Energy's National Nuclear Security Administration under contract DE-

NA0003525. The views expressed in the article do not necessarily represent the views of the U.S. DOE or the United States Government. We acknowledge the Core Center of Excellence in Nano Imaging (CNI) at USC for the use of their FIB and TEM instruments.

References

[1] Y. Ma, M.X. Yang, F.P. Yuan, X.L. Wu, A Review on Heterogeneous Nanostructures: A Strategy for Superior Mechanical Properties in Metals, Metals-Basel 9(5) (2019) 598.
[2] E. Ma, T. Zhu, Towards strength-ductility synergy through the design of heterogeneous nanostructures in metals, Mater Today 20(6) (2017) 323-331.
[3] X.L. Wu, Y.T. Zhu, Heterogeneous materials: a new class of materials with unprecedented mechanical properties, Mater Res Lett 5(8) (2017) 527-532.
[4] K. Lu, Making strong nanomaterials ductile with gradients, Science 345(6203) (2014) 1455.
[5] A.Y. Chen, J.B. Liu, H.T. Wang, J. Lu, Y.M. Wang, Gradient twinned 304 stainless steels for high strength and high ductility, Mat Sci Eng a-Struct 667 (2016) 179-188.
[6] Z. Cheng, L. Lu, The effect of gradient order on mechanical behaviors of gradient nanotwinned Cu, Scripta Mater 164 (2019) 130-134.
[7] Y. Lin, J. Pan, H.F. Zhou, H.J. Gao, Y. Li, Mechanical properties and optimal grain size distribution profile of gradient grained nickel, Acta Mater 153 (2018) 279-289.
[8] Z. Cheng, H. Zhou, Q. Lu, H. Gao, L. Lu, Extra strengthening and work hardening in gradient nanotwinned metals, Science 362(6414) (2018) eaau1925.
[9] Y.D. Gamburg, G. Zangari, Theory and practice of metal electrodeposition, Springer Science & Business Media2011.
[10] M.X. Yang, R.G. Li, P. Jiang, F.P. Yuan, Y.D. Wang, Y.T. Zhu, X.L. Wu, Residual stress provides significant strengthening and ductility in gradient structured materials, Mater Res Lett 7(11) (2019) 433-438.
[11] S.Q. Deng, A. Godfrey, W. Liu, N. Hansen, A gradient nanostructure generated in pure copper by platen friction sliding deformation, Scripta Mater 117 (2016) 41-45.
[12] K.S. Harsha, Principles of vapor deposition of thin films, Elsevier2005.
[13] J.A. Thornton, Influence of apparatus geometry and deposition conditions on the structure and topography of thick sputtered coatings, Journal of Vacuum Science and Technology 11(4) (1974) 666-670.
[14] G.D. Sim, J.A. Krogstad, K.Y. Xie, S. Dasgupta, G.M. Valentino, T.P. Weihs, K.J. Hemker, Tailoring the mechanical properties of sputter deposited nanotwinned nickel-molybdenum-tungsten films, Acta Mater 144 (2018) 216-225.
[15] K. Lu, Stabilizing nanostructures in metals using grain and twin boundary architectures, Nat Rev Mater 1(5) (2016) 16019.
[16] Y.F. Zhao, T.A. Furnish, M.E. Kassner, A.M. Hodge, Thermal stability of highly nanotwinned copper: The role of grain boundaries and texture, J Mater Res 27(24) (2012) 3049-3057.
[17] X. Zhang, A. Misra, Superior thermal stability of coherent twin boundaries in nanotwinned metals, Scripta Mater 66(11) (2012) 860-865.
[18] M.-A. Charpagne, J.-M. Franchet, N. Bozzolo, Overgrown grains appearing during sub-solvus heat treatment in a polycrystalline γ-γ'Nickel-based superalloy, Materials & Design 144 (2018) 353-360.
[19] G.A. He, L.M. Tan, F. Liu, L. Huang, Z.W. Huang, L. Jiang, Unraveling the formation mechanism of abnormally large grains in an advanced polycrystalline nickel base superalloy, J Alloy Compd 718 (2017) 405-413.
[20] G.A. He, F. Liu, L. Huang, Z.W. Huang, L. Jiang, Controlling grain size via dynamic recrystallization in an advanced polycrystalline nickel base superalloy, J Alloy Compd 701 (2017) 909-919.

[21] X. Wang, Z.W. Huang, B. Cai, N. Zhou, O. Magdysyuk, Y.F. Gao, S. Srivatsa, L.M. Tan, L. Jiang, Formation mechanism of abnormally large grains in a polycrystalline nickel-based superalloy during heat treatment processing, Acta Mater 168 (2019) 287-298.
[22] M. Detrois, K.A. Rozman, P.D. Jablonski, J.A. Hawk, Compositional Design and Mechanical Properties of INCONEL® Alloy 725 Variants, in: E. Ott, X. Liu, J. Andersson, Z. Bi, K. Bockenstedt, I. Dempster, J. Groh, K. Heck, P. Jablonski, M. Kaplan, D. Nagahama, C. Sudbrack (Eds.) Proceedings of the 9th International Symposium on Superalloy 718 & Derivatives: Energy, Aerospace, and Industrial Applications, Springer International Publishing, Cham, 2018, pp. 421-437.
[23] M.G. Emigh, R.D. McAuliffe, C.Q. Chen, J.C. Mabon, T. Weihs, K.J. Hemker, D.P. Shoemaker, J.A. Krogstad, Influence of a nanotwinned, nanocrystalline microstructure on aging of a Ni-25Mo-8Cr superalloy, Acta Mater 156 (2018) 411-419.
[24] L. Velasco, A.M. Hodge, Growth twins in high stacking fault energy metals: Microstructure, texture and twinning, Mat Sci Eng a-Struct 687 (2017) 93-98.
[25] J.A. Bahena, J.S. Riano, M.R. Chellali, T. Boll, A.M. Hodge, Thermally activated microstructural evolution of sputtered nanostructured Mo–Au, Materialia 4 (2018) 157-165.
[26] J.S. Riano, A.M. Hodge, Exploring the microstructural evolution of Hf-Ti: From nanometallic multilayers to nanostructures, Scripta Mater 142 (2018) 55-60.
[27] G. Abadias, E. Chason, J. Keckes, M. Sebastiani, G.B. Thompson, E. Barthel, G.L. Doll, C.E. Murray, C.H. Stoessel, L. Martinu, Review Article: Stress in thin films and coatings: Current status, challenges, and prospects, J Vac Sci Technol A 36(2) (2018) 020801.
[28] A.J. Detor, A.M. Hodge, E. Chason, Y. Wang, H. Xu, M. Conyers, A. Nikroo, A. Hamza, Stress and microstructure evolution in thick sputtered films, Acta Mater 57(7) (2009) 2055-2065.
[29] R. Daniel, J. Keckes, I. Matko, M. Burghammer, C. Mitterer, Origins of microstructure and stress gradients in nanocrystalline thin films: The role of growth parameters and self-organization, Acta Mater 61(16) (2013) 6255-6266.
[30] J.A. Thornton, D.W. Hoffman, Stress-related effects in thin films, Thin Solid Films 171(1) (1989) 5-31.
[31] V.M. Miller, A.E. Johnson, C.J. Torbet, T.M. Pollock, Recrystallization and the Development of Abnormally Large Grains After Small Strain Deformation in a Polycrystalline Nickel-Based Superalloy, Metall Mater Trans A 47a(4) (2016) 1566-1574.
[32] A. Agnoli, M. Bernacki, R. Logé, J.-M. Franchet, J. Laigo, N. Bozzolo, Selective growth of low stored energy grains during δ sub-solvus annealing in the Inconel 718 nickel-based superalloy, Metallurgical and Materials Transactions A 46(9) (2015) 4405-4421.
[33] T.A. Bennett, P.N. Kalu, A.D. Rollett, Strain-induced selective growth in 1.5% temper-rolled Fe∼ 1% Si, Microscopy and Microanalysis 17(3) (2011) 362-367.
[34] R. Treml, D. Kozic, J. Zechner, X. Maeder, B. Sartory, H.P. Gänser, R. Schöngrundner, J. Michler, R. Brunner, D. Kiener, High resolution determination of local residual stress gradients in single-and multilayer thin film systems, Acta Mater 103 (2016) 616-623.
[35] F.J. Humphreys, Recrystallization and Related Annealing Phenomena, 2017.
[36] G.S. Rohrer, Grain boundary energy anisotropy: a review, Journal of materials science 46(18) (2011) 5881-5895.
[37] S.P. Hau-Riege, C.V. Thompson, In situ transmission electron microscope studies of the kinetics of abnormal grain growth in electroplated copper films, Applied Physics Letters 76(3) (2000) 309-311.
[38] D.G. Morris, S. Naka, P. Caron, Intermetallics and superalloys, Deutsche Gesellschaft für Materialkunde2000.
[39] M. Durand-Charre, The microstructure of superalloys, Routledge2017.
[40] X. Zhou, X.-x. Yu, T. Kaub, R.L. Martens, G.B. Thompson, Grain boundary specific segregation in nanocrystalline Fe (Cr), Scientific reports 6 (2016) 34642.
[41] H.R. Peng, M.M. Gong, Y.Z. Chen, F. Liu, Thermal stability of nanocrystalline materials: thermodynamics and kinetics, International materials reviews 62(6) (2017) 303-333.
[42] J.L. Bair, S.L. Hatch, D.P. Field, Formation of annealing twin boundaries in nickel, Scripta Mater 81 (2014) 52-55.
[43] C.M. Barr, A.C. Leff, R.W. Demott, R.D. Doherty, M.L. Taheri, Unraveling the origin of twin related domains and grain boundary evolution during grain boundary engineering, Acta Mater 144 (2018) 281-291.
[44] N. Bozzolo, N. Souaï, R.E. Logé, Evolution of microstructure and twin density during thermomechanical processing in a γ-γ'nickel-based superalloy, Acta Mater 60(13-14) (2012) 5056-5066.

[45] A.M. Hodge, T.A. Furnish, C.J. Shute, Y. Liao, X. Huang, C.S. Hong, Y.T. Zhu, T.W. Barbee Jr, J.R. Weertman, Twin stability in highly nanotwinned Cu under compression, torsion and tension, Scripta Mater 66(11) (2012) 872-877.
[46] P.A. Beck, P.R. Sperry, Strain induced grain boundary migration in high purity aluminum, Journal of applied physics 21(2) (1950) 150-152.
[47] T.S. Prithiv, P. Bhuyan, S.K. Pradhan, V.S. Sarma, S. Mandal, A critical evaluation on efficacy of recrystallization vs. strain induced boundary migration in achieving grain boundary engineered microstructure in a Ni-base superalloy, Acta Mater 146 (2018) 187-201.
[48] N. Ratel, G. Bruno, P. Bastie, T. Mori, Plastic strain-induced rafting of γ′ precipitates in Ni superalloys: Elasticity analysis, Acta Mater 54(19) (2006) 5087-5093.
[49] M. Kamaraj, Rafting in single crystal nickel-base superalloys—an overview, Sadhana 28(1-2) (2003) 115-128.
[50] J.D. Nystrom, T.M. Pollock, W.H. Murphy, A. Garg, Discontinuous cellular precipitation in a high-refractory nickel-base superalloy, Metallurgical and Materials Transactions A 28(12) (1997) 2443-2452.
[51] E.W. Huang, P.K. Liaw, High-temperature materials for structural applications: New perspectives on high-entropy alloys, bulk metallic glasses, and nanomaterials, MRS Bulletin 44(11) (2019) 847-853.
[52] M. Sundararaman, P. Mukhopadhyay, S. Banerjee, Precipitation of the δ-Ni 3 Nb phase in two nickel base superalloys, Metallurgical transactions A 19(3) (1988) 453-465.
[53] S. Azadian, L.-Y. Wei, R. Warren, Delta phase precipitation in Inconel 718, Materials characterization 53(1) (2004) 7-16.
[54] Y. Mei, Y. Liu, C. Liu, C. Li, L. Yu, Q. Guo, H. Li, Effects of cold rolling on the precipitation kinetics and the morphology evolution of intermediate phases in Inconel 718 alloy, J Alloy Compd 649 (2015) 949-960.
[55] B. Hassan, J. Corney, Grain boundary precipitation in Inconel 718 and ATI 718Plus, Mater Sci Tech-Lond 33(16) (2017) 1879-1889.
[56] C.C. Koch, R.O. Scattergood, M. Saber, H. Kotan, High temperature stabilization of nanocrystalline grain size: thermodynamic versus kinetic strategies, J Mater Res 28(13) (2013) 1785-1791.
[57] L.E. Shoemaker, Alloys 625 and 725: trends in properties and applications, Superalloys 718(625) (2005) 409-418.
[58] M. Anderson, A.L. Thielin, F. Bridier, P. Bocher, J. Savoie, δ Phase precipitation in Inconel 718 and associated mechanical properties, Materials Science and Engineering: A 679 (2017) 48-55.
[59] B.B. Zhang, F.K. Yan, M.J. Zhao, N.R. Tao, K. Lu, Combined strengthening from nanotwins and nanoprecipitates in an iron-based superalloy, Acta Mater 151 (2018) 310-320.
[60] N.M. Heckman, L. Velasco, A.M. Hodge, Influence of Twin Thickness and Grain Size on the Tensile Behavior of Fully Nanotwinned CuAl Alloys Advanced Engineering Materials 18(6) (2016) 918-922.
[61] P.F. Wang, Z. Han, K. Lu, Enhanced tribological performance of a gradient nanostructured interstitial-free steel, Wear 402-403 (2018) 100-108.
[62] L.M. Tan, Z.W. Huang, F. Liu, G.A. He, X. Wang, L. Huang, Y.W. Zhang, L. Jiang, Effects of strain amount and strain rate on grain structure of a novel high Co nickel-based polycrystalline superalloy, Materials & Design 131 (2017) 60-68.

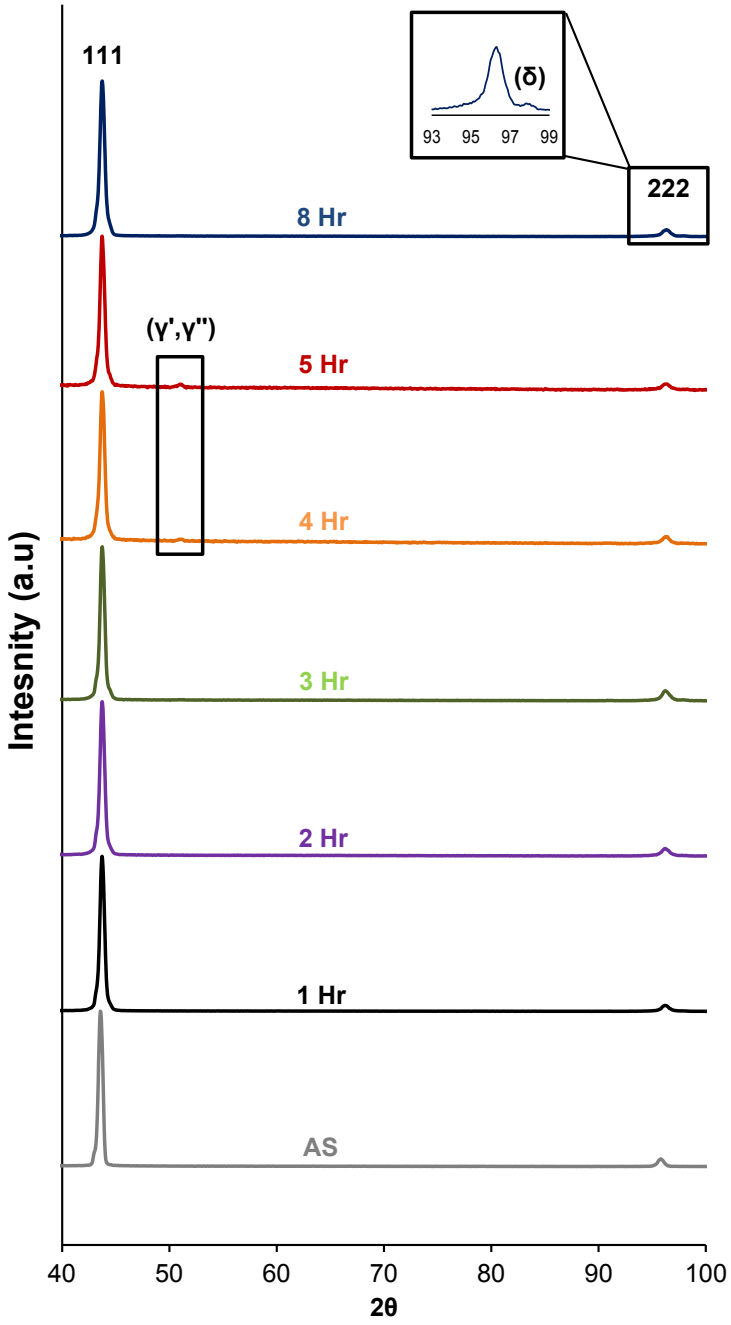

Supplementary Data S1. XRD data of samples annealed at 730˚C at various aging times, collected on a Rigaku Ultima IV diffractometer. The boxes highlight structural changes.